Two-dimensional modelling of the dielectric barrier discharge in air

Plasma Sources Sci. Technol. 1 (1992) 166–174 Printed in the UK

Two-dimensional modelling of the dielectric barrier discharge in air

Dieter Braun, Valentin Gibalov† and Gerhard Pietsch

Grundgebiete der Elektrotechnik und Gasentladungstechnik, Aachen University of Technology (RWTH Aachen), Schinkelstraße 2, D-5100 Aachen, Federal Republic of Germany

Received 13 January 1992, in final form 20 July 1992

Abstract. A self-consistent two-dimensional modelling of microdischarges in devices in which one of the electrodes is covered with a dielectric is presented. The discharge development can be divided into four phases, a Townsend, an ionization wave or streamer, a cathode layer formation, and a decay phase. While during the Townsend phase the initial field strength distribution is hardly distorted, an ionization wave propagates towards the cathode during the following phase. On the wave reaching the cathode, a cathode layer develops. Its radial extension is determined by the increase of the current. During the decay phase the distributions of, for example, field strength and charge carriers are nearly frozen. The discharge fades because of the slow decrease of the field strength within its column. Energy and temperature distributions of microdischarge channels in air at atmospheric pressure are given.

1. Introduction

Barrier discharge occurs when an alternating high voltage is applied to conductive electrodes, at least one of which is covered with a dielectric layer. When the breakdown field strength is reached in the gas gap, the discharge ignites. On extended electrodes at atmospheric pressure, the discharge current flows through several microdischarge channels, randomly distributed in time and space on the surfaces of the electrodes. The dielectric layer limits the current and allows microdischarges to burn simultaneously. Owing to the dielectric layer, the current pulses last for several tens of nanoseconds. The accumulation of charge carriers on the dielectric surface reduces the mean field strength in the gap and extinguishes the discharge. The microdischarges behave like transient high-pressure glow discharges. They have been investigated in detail experimentally [1–4]. Creep discharges have been detected on the dielectric surface.

Because of the properties of this non-equilibrium discharge type there exist wide fields of possible applications in plasma chemistry, such as in ozonizers, in excimer lamps and for removal of waste gases. In high-voltage techniques, this discharge type is called partial discharge and its occurrence is the reason for limited lifetimes of insulating materials.

In order to improve the features of barrier discharges for application purposes, a detailed knowledge of their properties is necessary. For this purpose, modelling of the discharge development has been performed [2, 3, 5, 6]. One-dimensional modelling does not reveal the radial features of the discharge [5]. In order to overcome this problem, a limited column size was taken into account as well as the propagation of charges on the dielectric surface in [2]. In [6], a two-dimensional attempt was undertaken, without taking into account secondary electron production at the cathode. The two-dimensional modelling mentioned in [3] is based on the assumption that the ion drift is zero. However, ion drift is essential for cathode layer formation. Taking into account this effect, a two-dimensional, self-consistent description of the development of the barrier discharge is presented. The model is described in section 2. The dynamic behaviour of the discharge is analysed in sections 3 to 5, while in section 6 some energetic features of the discharge channel are presented.

2. Model

2.1. Equations

By solving the Boltzmann equations in the form of continuity equations for different species together with the Poisson equation, the spatial and temporal distributions of field strength and particle concentrations within the discharge channel can be obtained.

† Permanent address: Chemical Department, Moscow State University, 119899, Moscow, Russia

0963-0252/92/030166+09 $07.50

$$\frac{\delta n_i(r,t)}{\delta t} + \mathrm{div}\{n_i(r,t)\cdot v_i(E/n)\} - \mathrm{div}\{D_i\cdot \mathrm{grad}(n_i(r,t))\}$$

$$= S_i(n_1,\ldots,n_m) \qquad (1)$$

$i = N_2^+$, O_2^+, O_2^-, O^-, O, electrons and so on, where $n_i(r,t)$ is the concentration of the ith particle, $v_i(E/n)$ the drift velocity, E/n the reduced electric field strength, r the space coordinate and $S_i(n_1,\ldots,n_m)$ the production terms. The production terms describe interaction between different particles. The list of reactions considered is given in [2]. D_i is the (perpendicular) diffusion coefficient.

Assuming cylindrical symmetry, r consists of two coordinates. E/n follows from the Poisson equation

$$\Delta\Phi(r,t) = -\rho(r,t)/\varepsilon_0 \qquad (2)$$

in connection with

$$E(r,t) = -\mathrm{grad}\,\Phi(r,t) \qquad (3)$$

where $\Phi(r,t)$ is the electric potential, $\rho(r,t)$ the total charge density and ε_0 the dielectric constant.

2.2. Initial and boundary conditions

The following initial conditions were chosen: (1) all particle concentrations, except those of the nitrogen and oxygen molecules, are taken to be zero; (2) the initial electrons at the cathode are distributed according to a Gauss curve, in both radial and longitudinal direction; the width of these distributions is several micrometres; (3) the total number of electrons in this cloud is varied between 100 and 10^6; and (4) the initial electric field strength distribution is uniform, its value slightly above the break-down one.

Barrier discharge arrangements have at least three boundaries, two conductive and one dielectric (figure 1). The anode (of infinite size) is covered with a dielectric. On the boundaries in the discharge gap, it is necessary to define boundary conditions for the charged particles and the potentials.

Charged particles hitting the dielectric surface are adsorbed. The electron current on the cathode is considered to be caused by ion current and photon flux:

$$j_e = \gamma_{ion} j_{ion} + \gamma_{ph} j_{ph} \qquad (4)$$

where j_e, j_{ion} and j_{ph} are the electron, positive ion and photon current densities respectively; γ_{ion} and γ_{ph} are the corresponding second Townsend ionization coefficients.

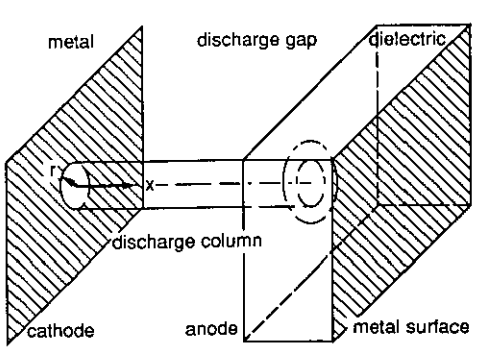

Figure 1. Principle of the discharge arrangement.

The potential on the conductive cathode is taken as zero, on the conductive anode as constant. Its value (V) is determined by the breakdown field strength in the air gap:

$$\Phi(0,r,t) = 0 \qquad \Phi(d+D,r,t) = V \qquad (5)$$

where d is the gap width and D the thickness of the dielectric layer. On the dielectric surface the following boundary relations apply:

$$E_z(d^-,r,t) = \varepsilon_D E_z(d^+,r,t) + \sigma(r,t)/\varepsilon_0 \qquad (6)$$

$$E_r(d^-,r,t) = E_r(d^+,r,t) \qquad (7)$$

where E_z and E_r are the axial and radial components of the electric field strength; σ is the surface charge density; and d^- and d^+ the dielectric surface coordinates at the gas and dielectric sides respectively. Far from the channel axis, the electric field strength is considered to be uniform.

All calculations were performed for an air pressure of 1 bar, a discharge gap of 1 mm, and a dielectric thickness of 3 mm. The relative dielectric constant ε_D was usually 5.

2.3. Numerical procedure

In order to obtain the numerical solution of the system of equations (1)–(3) with the initial and boundary conditions (4)–(7), the system was transformed into algebraic equations on a two-dimensional space grid. The cell size of this grid was variable. In the radial direction the distance between two grid points increases exponentially with radius. In the axial direction this distance is reduced to less than 1 μm near the cathode and then increases towards the anode. The number of cells was limited to between 60 and 250 in both dimensions.

A brief description of the numerical procedure is presented in figure 2. The value of the actual time step chosen was dependent on grid distance and drift velocity. Each time step is divided into several sub-steps (figure 2). During the first one, the movement of particles (convection and diffusion) is regarded as being frozen, and the modification of concentrations during Δt caused by the source terms of the continuity equations is computed. During the second step, charge carrier movement is calculated without particle production. During the third step, physical diffusion is considered and the numerical diffusion is corrected with the help of a flux-correction transport technique [7]. The field configuration for the modified charged particle distribution is obtained in the last sub-step. It is calculated directly within the whole region of integration including the dielectric volume with a program package given in [8, 9].

In order to verify the developed numerical model, test runs have been undertaken. In particular, the influence of the cell diffusion at different initial electron distributions has been tested. Comparing the obtained results with analytical solutions, the numerical error was found not to exceed a level of 2–5%.

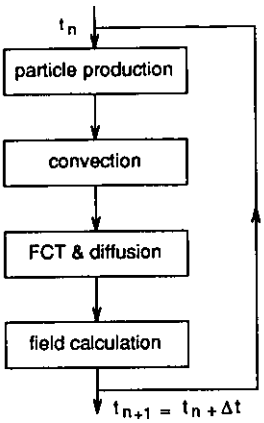

Figure 2. Simplified flow chart of the routine.

3. Initial stages of break-down

Modelling the development of the discharge, one can distinguish four phases. The discharge starts with electrons drifting from the cathode to the anode. The electron multiplication is determined by Townsend's first ionization coefficient (the Townsend phase). When a certain level of electron density is reached, a significant field distortion appears and causes a cathode-directed ionization wave (the streamer phase). When the streamer reaches the cathode, a cathode layer develops (the cathode-layer formation phase). Finally, depending on the dielectric layer properties, the current through the discharge column decays (the decay phase).

The calculations start with initial electrons near the cathode ($t = 0$), which begin to move to the anode. During their drift to the anode, they collide with neutral particles, ionizing them and thus multiplying the number of charged species. Together with the generated ions, photons and detached electrons from negative ions, they cause a low initial current. Up to a certain level of electron concentration, the multiplication factor is constant, in accordance with the Townsend mechanism at constant electric field strength.

The current during the Townsend phase results in an accumulation of charge carriers near the anode and electron collection on the dielectric surface. The accumulated charged particles distort the field distribution near the anode and thereby enhance the conductivity. In this region the field strength decreases, while it increases in the cathode direction. The amplitude of the distortion increases with time and a new process starts.

Electrons generated at the cathode or by detachment processes between the cathode and the field distortion peak, drift in regions of higher electric field strength than during the Townsend phase. This leads to a further accumulation of charge carriers at the position of the field distortion peak, raising the conductivity in this region, thus shifting and enlarging the distortion towards the cathode. This is a self-amplifying effect resulting in a cathode-directed ionization wave or streamer.

In the region between the ionization wave maximum and the anode, the field strength is reduced to a stable level at which the value of the effective ionization coefficient is nearly zero, covering mainly the charge losses.

The radial extension of the discharge in the initial phases is mainly determined by electron diffusion. From the initial Gauss distribution of the electron density with a radius of about several micrometres, a diameter of about 100 μm is reached at the anode. The first steps of the streamer propagation are governed by diffusion, too. When the streamer head approaches the cathode, an interaction between radiation from the streamer head and the cathode surface appears. The size of the irradiated cathode area is significantly wider than the cross section of the streamer head (figure 3 [10]).

The general picture of the initial phases of the discharge developed in this section is confirmed by calculation results given in figures 4 and 5. In figure 4 the simulation of streak photographs of the discharge development is presented. Such photographs are obtained if a

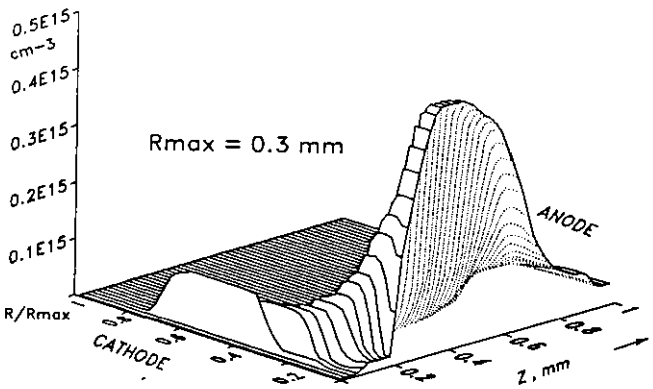

Figure 3. Electron density distribution at $t = 7.5$ ns (after the start of the initial seed electrons).

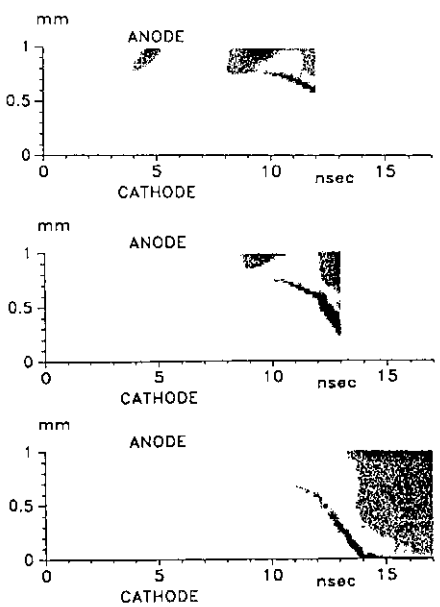

Figure 4. Simulation of a streak photograph, the sensitivity of the bottom photographs is five and five hundred times, respectively, less than that of the upper one (see text).

film is moved rapidly, perpendicular to the axis of the propagating channel. The intensity of the radiation is given by the density of points. It follows from an integration over the line of sight. The radiation is taken as proportional to the absolute amount of ionization processes of the corresponding cross section.

The initial electrons start at $t = 0$ from the cathode. At time 3.5 ns later, radiation from the avalanches propagating to the anode is detected (figure 4, top). It belongs to the Townsend phase of the discharge. After the accumulation of charge carriers near the anode, a field strength distortion happens, and at about 10 ns the beginning of the cathode-directed streamer can be detected. The simulation in the top part of figure 4 is stopped at 12 ns. Reducing the sensitivity of the simulated photograph by a factor of five (figure 4, middle) and

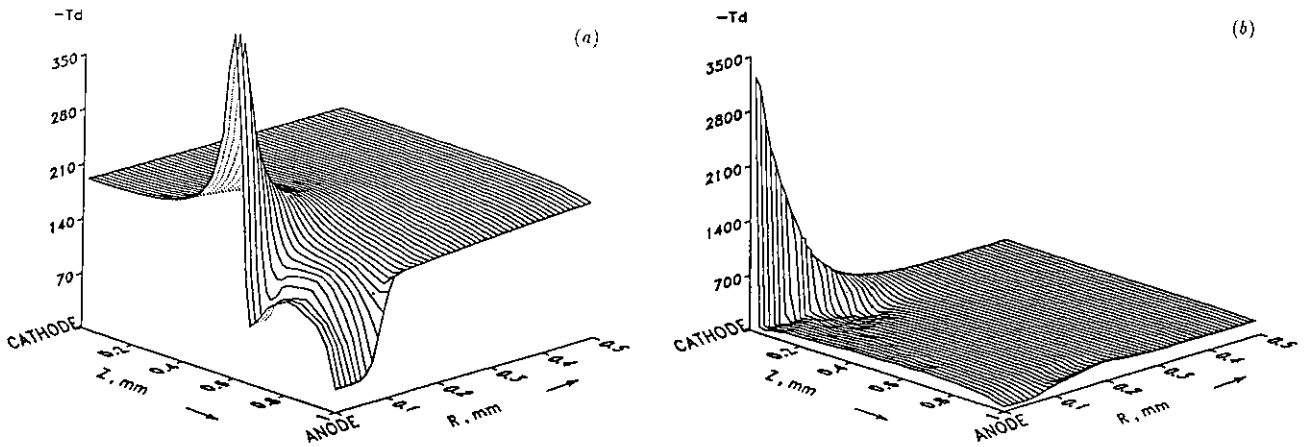

Figure 5. Axial field strength distribution at moments when the streamer increases its velocity significantly (*a*) and when the streamer head reaches the cathode (*b*).

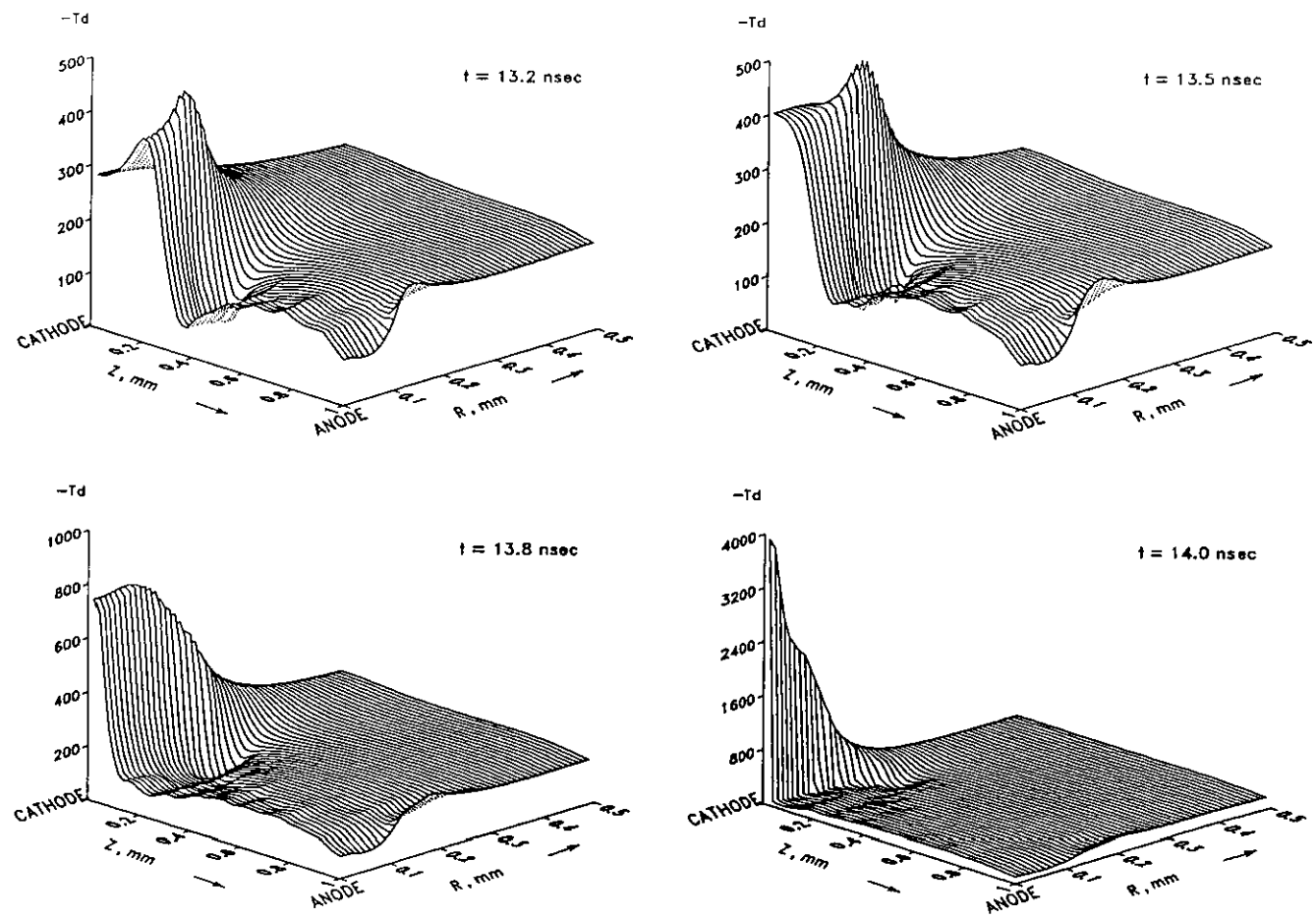

Figure 6. Axial electric field strength during cathode layer formation at different time steps.

500 (figure 4, bottom) the simulation is performed up to 13 ns and 15 ns respectively. The cathode-directed streamer with accelerating propagation velocity is seen up to the cathode. The simulated discharge pattern is rather similar to experimental ones, even regarding the dark space between column and cathode [2, 11].

In figure 5 the axial field strength distortion and its propagation towards the cathode are demonstrated at two instants, at 12 ns (figure 5(*a*)) when the propagation speed is increased significantly (see figure 4), and at 13.9 ns (figure 5(*b*)). At 13.9 ns the streamer reaches the cathode. The field strength is dramatically increased up to several thousand Townsend. This is the starting point of the cathode layer formation.

4. Cathode layer formation

The field strength increase in front of the cathode occurs in less than 1 ns under the given conditions (figure 6). The field strength distribution as well as those of the ion and electron concentrations are compressed during this process, that is the appropriate thickness of the cathode layer becomes of the order of 10 μm. This value is strongly influenced by the effective ionization coefficient. The value of the reduced field strength finally reaches more than 4000 Townsend.

The rise of the positive ion density at the cathode, resulting from the compression process, causes a significant increase of the electron emission current.

As follows from the modelling, nearly simultaneously with cathode layer formation, the cathode layer extends radially (figure 7). This is connected with a further current increase. A current increase means an enlargement of the ion and electron concentration in the cathode fall. By this the radial component of the field strength on the radial boundary is increased, too (figure 8). This is the reason for the radial extension of the cathode layer.

During the cathode layer formation the current density at the external boundary of the layer is nearly constant, about 250 A cm^{-2}. From this it follows that the rate of rise of the external current is connected with the velocity of extension of the cathode layer area (and not the drift velocity of charged particles). The current

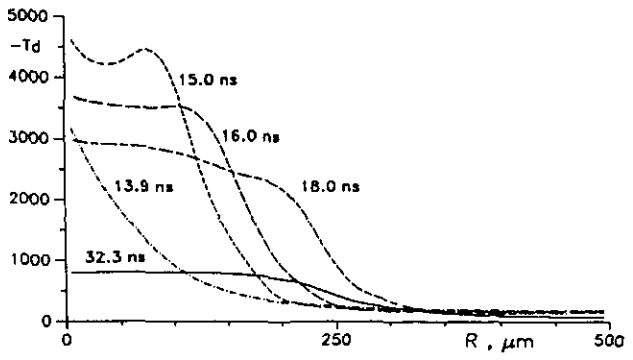

Figure 7. Radial distribution of the axial field strength on the cathode.

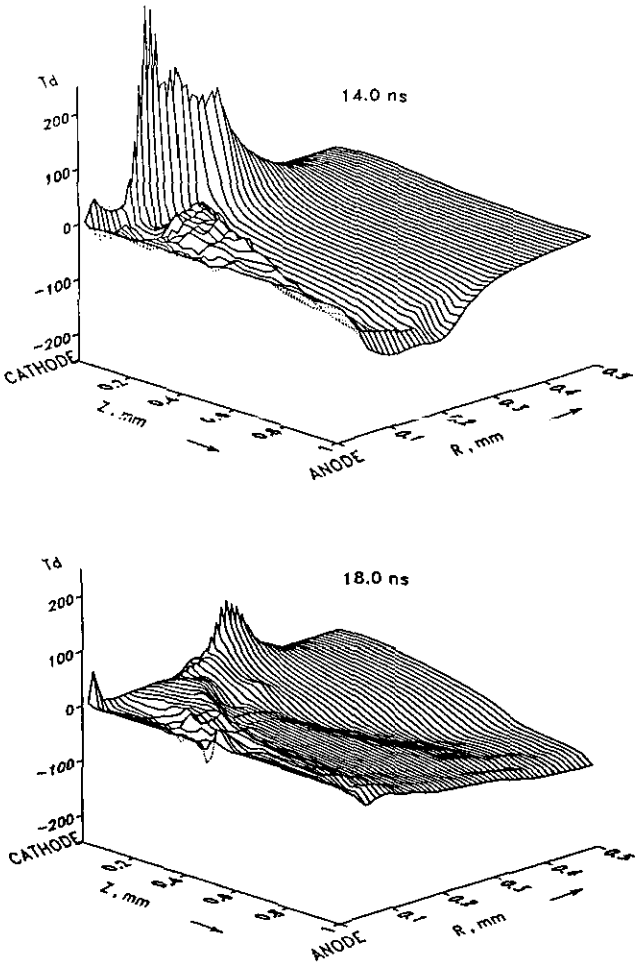

Figure 8. Radial field strength distributions before (14.0 ns) and at current peak (18.0 ns).

maximum value is about 100 mA and occurs approximately 18 ns after the appearance of the initial electrons.

The velocity of the radial propagation of the layer decreases when the current reaches its maximum. Near the current maximum, the cathode layer formation is completed (figure 9). From this point all distributions at the cathode and that in the channel are nearly frozen. After the current peak, the adsorbed charge on the dielectric (anode) causes a slow decrease of the current density (at the axial boundary) of the cathode layer to 60 to 80 A cm^{-2}.

The thickness of the cathode layer corresponds to about 1 mbar cm (figure 9). This value depends on the attachment coefficient, for figure 9 a value five times lower than the value given in the literature [14] has been chosen. This reduction causes a factor of 1.5 decrease in the layer width. The cathode fall is about 600 V. A change in the dielectric constant from 5 to 50 alters the radius of the cathode layer from about 200 to 600 μm and hence alters only its radial propagation time.

5. Discharge decay

Up to the decay phase, the conditions on the anode do not influence the discharge development, provided that

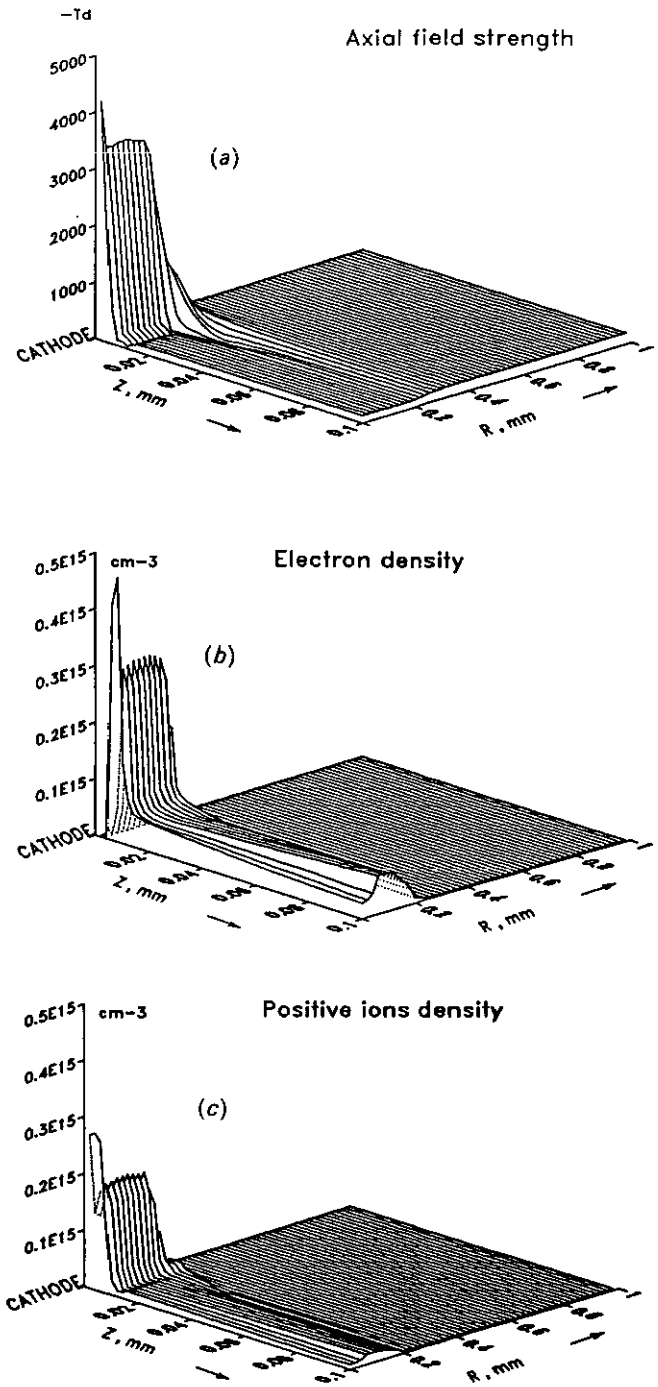

Figure 9. Characteristic distributions in the cathode layer at current peak ($t = 18$ ns), (*a*) axial field strength, (*b*) electron density, and (*c*) positive ion density.

the initial field strength in the discharge gap is similar. During the Townsend, streamer and cathode-layer formation phases the discharge development is governed by the same mechanisms despite the type of the anode (dielectric or metal).

The current flow through the column during the decay phase is determined by the ability of the cathode layer to carry current and by the external circuit (the wiring and the properties of the dielectric in the case of a barrier discharge). During this phase the current peak occurs.

With a dielectric anode, the current flow through the column leads to a significant surface charge density on the dielectric surface (a maximum about 20 nC cm^{-2} for the given conditions). This surface charge reduces the mean channel electric field strength, stops the radial extension of the cathode layer and determines the field configuration in front of the anode. A significant radial electric field strength (up to about 100 Td, figure 8), appears around the surface charge. Owing to the accumulation of adsorbed charges, the mean electric field strength slowly decreases within the column. Simultaneously with this decrease, the current declines and finally fades. Calculated and measured current shapes and the values of the transferred charge dhring a discharge pulse are in close agreement [15].

The diameter of the discharge column is strongly related to the area on the cathode where electrons are emitted. It practically defines the diameter of the discharge channel except in the anode region. The calculated radius is about 200 μm, in sufficient accordance with measured values [2]. Near the anode, repulsion forces of electrons, as well as accumulated charges on the surface, cause an increase of the diameter. As a result, circular surface discharges appear.

The main part of the dissipated discharge energy occurs during the decay phase (figure 10). The mean electron energy is about 2 eV. This follows from the mean electric field strength of about 80 Td [16] (figure 11(*a*)) and is in good agreement with experimental findings [12]. Beside the cathode region, the maximum energy happens in the midst of the gap in correlation with the electron density distribution (figure 11(*b*)).

During the discharge decay phase, the electric field strength at the cathode drops, the cathode layer thickness increases and the average field strength in the discharge column reduces to about 30 to 40 Td.

6. Energy and temperature in the discharge channel

In the decay phase, the energy density distribution resembles that given in figure 12 [13]. There exist two maxima: one in the cathode layer and another in the midst of the discharge channel. The maximum value depends, among other factors, on the dielectric constant; for $\varepsilon_D = 5$ and 50 it is 370 and 800 mJ cm^{-3} respectively.

As the energy density is proportional to temperature (the thermal capacity of air at normal conditions is about 0.9 mJ cm^{-3}), figure 12 is representative for the temperature distribution within the discharge channel as well. In the cathode layer, local overtemperatures of about 400 K (for $\varepsilon_D = 5$) occur.

The respective portions of energy carried by electrons and ions change during the course of the discharge. At the beginning, practically the total energy from the electric field is transferred to the discharge column by electrons. After cathode layer formation, in which the electron concentration is nearly zero, the energy transferred by ions becomes remarkable (figure 10). Energy

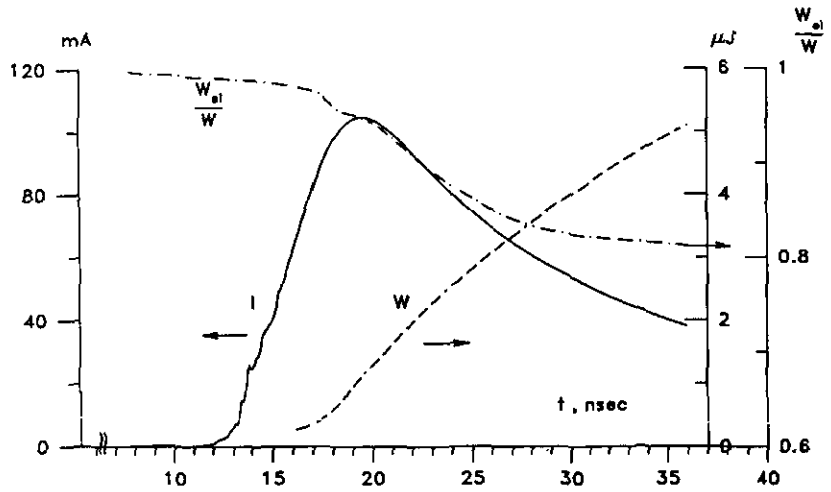

Figure 10. Current, energy and related electron energy of a microdischarge.

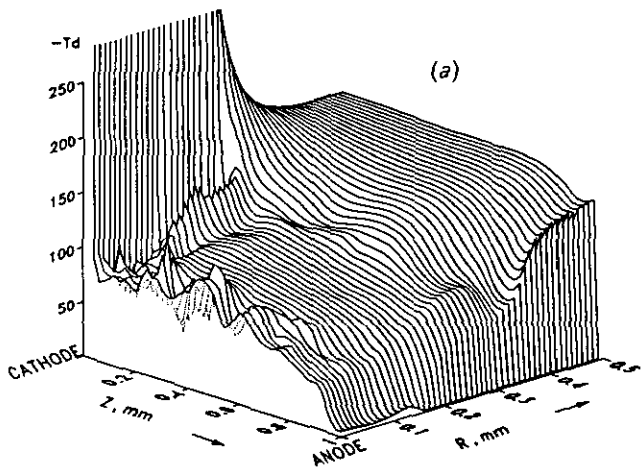

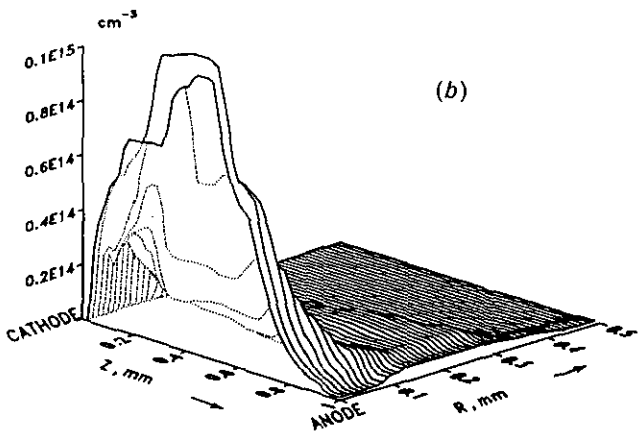

Figure 11. Axial field strength (*a*), and electron density (*b*) at current maximum ($t = 18$ ns).

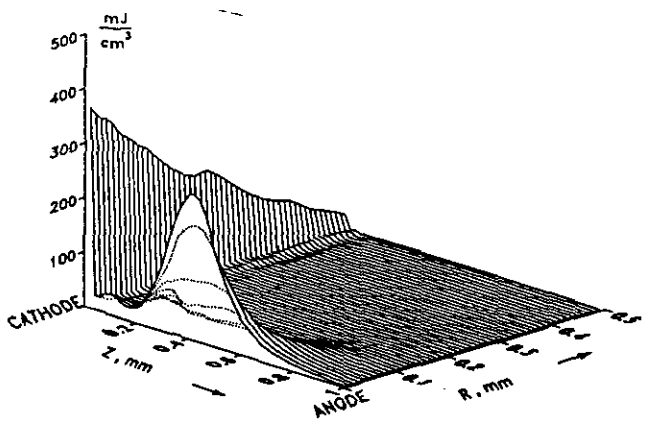

Figure 12. Energy density distribution at $t = 32.3$ ns.

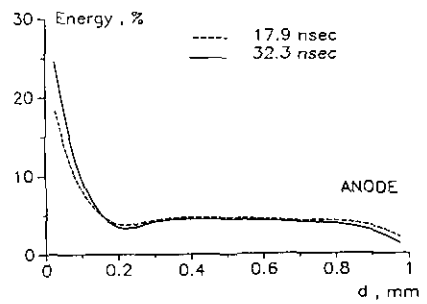

Figure 13. Relative energy content distributions integrated over slices of the discharge column with thickness 50 μm.

transfer by ions happens mainly in the cathode layer.

Integrating the energy content within slices of the column of 50 μm width gives the energy content distribution within the discharge channel. This distribution (related to the overall energy) is given in figure 13 at maximum current and at another moment during the further decay of the discharge. About 50% of the total energy is distributed within 20% of the discharge length at the cathode. Within about 80% of the column length, *the energy content is distributed almost homogeneously.*

The corresponding temperature distribution (averaged temperatures over the cross section) looks similar and is given in figure 14 [13]. The mean overtemperature in the column is about 5 K and reaches a maximum on the cathode of 200 K for a dielectric constant of $\varepsilon_D = 5$. At $\varepsilon_D = 50$ these values are 25 and 800 K respectively.

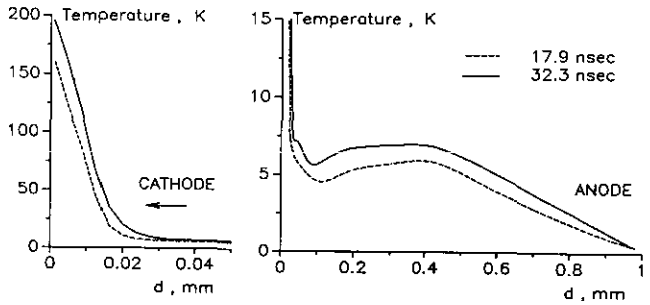

Figure 14. Axial distribution of the mean channel overtemperature at peak current (17.9 ns) and during the decay phase of the discharge at 32.3 ns.

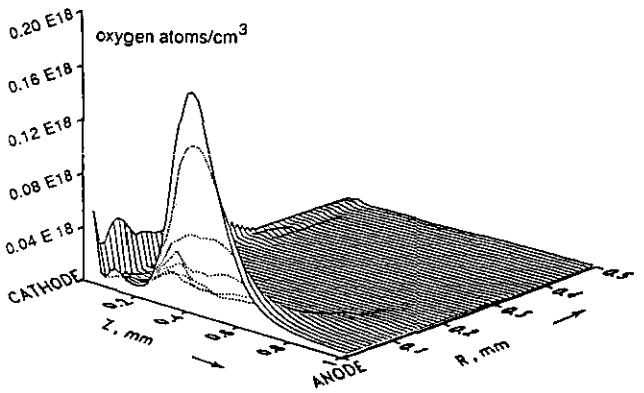

Figure 15. Atomic oxygen density distribution at $t = 32.3$ ns.

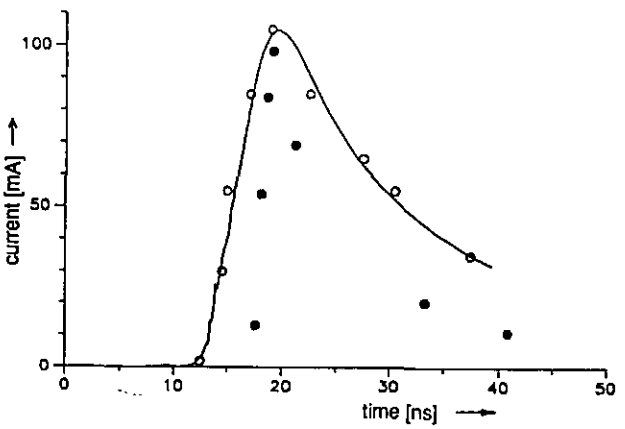

Figure 16. Comparison of calculated (full line) and measured (symbols) microdischarge currents. The measured values follow from similar boundary conditions (●: 1.2 bar instead of 1 bar [14], ○: 4 mm discharge gap [17]; the measured values are divided by 4).

7. Discussion and conclusion

From the modelling, it follows that four phases can be distinguished during barrier discharge development, a Townsend, a streamer, a cathode-layer formation and a decay phase. It is important to note that the build-up of a cathode fall is necessary even in barrier discharges, in order to carry the current flow. The discharge behaviour during the first three phases is independent of the dielectric at the given conditions.

After cathode-layer formation, further discharge development does not depend on the previous phases of the discharge. In particular it is independent of the number and distribution of the initial electrons. This is confirmed by numerical results and experimental findings on the value of the transferred charge. If one of the electrodes is conductive, a change of the polarity (and thereby number of initial electrons) hardly influences its value.

Though the mean electron energy is comparatively high during the first phases, the main amount of energy is released in the decay phase with a mean electron energy of about 2 eV. The barrier discharge is an example of a non-equilibrium discharge type which can be applied to initiate chemical reactions.

With knowledge of the distributions of energy density, temperature, field strength, electron concentration and energy, it is possible to calculate the yield of reactions which can be performed with barrier discharges. As an example, for the first step of ozone generation, the atomic oxygen density distribution is given in figure 15. It is similar to that of the energy density (figure 12) except at the cathode region. The energy density in the cathode layer is mainly determined by ions which are not able to dissociate molecular oxygen.

The maximum of the atomic oxygen density is found in the middle of the discharge gap, where the electron concentration is high, too (figure 11(*b*)). It exists, though there is a low efficiency of the ozone synthesis process, because of a low mean electric field strength in this region (figure 11(*a*)) which gives rise to a relatively low rate of oxygen dissociation by electron collisions.

The presented results of the two-dimensional, self-consistent modelling are in good agreement with experimental findings such as the current shape and value (figure 16), amount of transferred charge [15], diameter of the discharge channel [2] and streak photographs [2]. The modelling reveals details of the behaviour of the barrier discharge and can be taken as a basis for barrier discharge applications.

Acknowledgment

The authors gratefully acknowledge the valuable help of C Stangenberg during the performance of the calculations.

References

[1] Samoilovich V G, Gibalov V I and Kozlov K V 1989 *Physical Chemistry of the Barrier Discharge* (Moscow: Moscow State University) [in Russian]
[2] Braun D, Küchler U and Pietsch G J 1991 *J. Phys. D: Appl. Phys.* **24** 564–72
[3] Eliasson B and Kogelschatz U 1991 *IEEE Trans. Plasma Sci.* **PS-19** 309–23
[4] Tanaka M, Yagi S and Tabata N 1978 *Trans. IEE Japan* **98A** 57–62
[5] Yoshida K and Tagashira H 1986 *Mem. Kitami Inst. Technol.* **18** 11–20

[6] Gibalov V I, Samoilovich V G and Filippov Yu V 1981 *Russ. J. Phys. Chem.* **55** 471–9
[7] Boris J P and Book D L 1976 *Methods in Computational Physics* ed J Killeen (New York: Academic) pp 85–129
[8] Adams J, Swartztrauber P and Sweet R 1988 *FISHPAK: A Package of Fortran Subprograms for the Solution of Separable Elliptic Partial Differential Equations* (Boulder: University Corporation for Atmospheric Research)
[9] Swartztrauber P and Sweet R 1979 *ACM Trans. Math. Software* **5** 352–64
[10] Braun D, Gibalov V, Pietsch G J and Stangenberg C 1991 *XXth Int. Conf. Phen. Ionized Gases*, Pisa, Italy, Contributed Papers (Pisa: Istituto di Fisica Atomica e Molecolare) **6** 1245–6
[11] Heuser C and Pietsch G 1980 *Proc. 6th Int. Conf. Gas Discharges and their Applications* (IEE Conf. Publ. No 189) (London: IEE) pp 98–101
[12] Marode E 1975 *Appl. Phys.* **46** 2005–20
[13] Gibalov V I, Braun D and Pietsch G J 1991 *Proc. 10th Int. Symp. on Plasma Chem.*, Bochum, Germany (International Union of Pure and Applied Chemistry) **3** paper 3.2-7 pp 1–6
[14] Schulz P 1968 *Elektronische Vorgänge in Gasen und Festkörpern* (Karlsruhe: Braun)
[15] Küchler U P 1990 *On the Optimization of Air-fed Ozonizers* doctoral thesis, Aachen University of Technology (in German)
[16] Braun D 1990 *On the Efficiency of Ozone Generators* doctoral thesis, Aachen University of Technology (in German)
[17] Heuser C 1984 *On the Ozone Generation in Electrical Discharges* doctoral thesis, Aachen University of Technology (in German)